TU Delft

Delft University of Technology

Seismoacoustic Coupled Signals From Earthquakes in Central Italy
Epicentral and Secondary Sources of Infrasound

Shani-Kadmiel, Shahar; Assink, Jelle D.; Smets, Pieter S.M.; Evers, Läslo G.

DOI
10.1002/2017GL076125

Publication date
2018

Document Version
Final published version

Published in
Geophysical Research Letters

Citation (APA)
Shani-Kadmiel, S., Assink, J. D., Smets, P. S. M., & Evers, L. G. (2018). Seismoacoustic Coupled Signals From Earthquakes in Central Italy: Epicentral and Secondary Sources of Infrasound. *Geophysical Research Letters*, *45*(1), 427-435. https://doi.org/10.1002/2017GL076125

Important note
To cite this publication, please use the final published version (if applicable).
Please check the document version above.

Copyright
Other than for strictly personal use, it is not permitted to download, forward or distribute the text or part of it, without the consent of the author(s) and/or copyright holder(s), unless the work is under an open content license such as Creative Commons.

Takedown policy
Please contact us and provide details if you believe this document breaches copyrights.
We will remove access to the work immediately and investigate your claim.

This work is downloaded from Delft University of Technology.
For technical reasons the number of authors shown on this cover page is limited to a maximum of 10.

AGU PUBLICATIONS

Geophysical Research Letters

RESEARCH LETTER
10.1002/2017GL076125

Key Points:
- Coupling of seismic-induced ground motions to infrasound may occur over a larger extent than previously described in scientific literature
- Sources of infrasound are detected when there is an atmospheric duct connecting them to a receiver
- Understanding seismoacoustic coupling is important for CTBT verification purposes

Supporting Information:
- Supporting Information S1

Correspondence to:
S. Shani-Kadmiel,
s.shanikadmiel@tudelft.nl

Citation:
Shani-Kadmiel, S., Assink, J. D., Smets, P. S. M., & Evers, L. G. (2018). Seismoacoustic coupled signals from earthquakes in central Italy: Epicentral and secondary sources of infrasound. *Geophysical Research Letters*, *45*, 427–435. https://doi.org/10.1002/2017GL076125

Received 20 OCT 2017
Accepted 13 DEC 2017
Accepted article online 19 DEC 2017
Published online 11 JAN 2018

©2017. The Authors.
This is an open access article under the terms of the Creative Commons Attribution-NonCommercial-NoDerivs License, which permits use and distribution in any medium, provided the original work is properly cited, the use is non-commercial and no modifications or adaptations are made.

Seismoacoustic Coupled Signals From Earthquakes in Central Italy: Epicentral and Secondary Sources of Infrasound

Shahar Shani-Kadmiel[1,2], Jelle D. Assink[2], Pieter S. M. Smets[1,2], and Läslo G. Evers[1,2]

[1]Department of Geoscience and Engineering, Faculty of Civil Engineering and Geosciences, Delft University of Technology, Delft, Netherlands, [2]R&D Department of Seismology and Acoustics, Royal Netherlands Meteorological Institute, De Bilt, Netherlands

Abstract In this study we analyze infrasound signals from three earthquakes in central Italy. The M_w 6.0 Amatrice, M_w 5.9 Visso, and M_w 6.5 Norcia earthquakes generated significant epicentral ground motions that couple to the atmosphere and produce infrasonic waves. Epicentral seismic and infrasonic signals are detected at I26DE; however, a third type of signal, which arrives after the seismic wave train and before the epicentral infrasound signal, is also detected. This peculiar signal propagates across the array at acoustic wave speeds, but the celerity associated with it is 3 times the speed of sound. Atmosphere-independent backprojections and full 3-D ray tracing using atmospheric conditions of the European Centre for Medium-Range Weather Forecasts are used to demonstrate that this apparently fast-arriving infrasound signal originates from ground motions more than 400 km away from the epicenter. The location of the secondary infrasound patch coincides with the closest bounce point to I26DE as depicted by ray tracing backprojections.

Plain Language Summary Underground explosions and earthquakes generate ground motions at the surface of the Earth and induce pressure fluctuations in the atmosphere. These fluctuations propagate through the atmosphere as inaudible sound called infrasound and are detected by pressure sensors hundreds of kilometers away. In this paper, we discuss how these detections can reveal information about the regions in which seismic energy radiated from underground sources couples to the atmosphere and generates infrasound. We convey a new understanding of this process and demonstrate that infrasound may originate from a much larger region and much farther away from the source than previously described in the scientific literature. Understanding the interaction of these two wavefields, seismic and infrasonic, is important for monitoring nuclear explosions, for example, but can also be used to evaluate the state of the atmosphere from naturally occurring sources like earthquakes and volcano eruptions.

1. Introduction

Seismic energy radiated from subsurface sources can couple to the atmosphere and generate low-frequency acoustic waves, known as *infrasound* (Arrowsmith et al., 2010; Cook, 1971; Donn & Posmentier, 1964; Walker et al., 2013). Specifically, seismic-to-infrasonic coupling at the ground-atmosphere interface is shown to occur over the epicentral region of an earthquake due to ground motions (Marchetti et al., 2016; Mutschlecner & Whitaker, 2005) and over mountain ranges away from the epicenter due to shaking of the topographic relief (Le Pichon et al., 2005, 2006). Evers et al. (2014) have shown that seismic waves from submarine earthquakes couple to the water column and generate hydroacoustical waves and that seamounts can diffract acoustic energy and couple to the atmosphere to generate infrasound under evanescent regime conditions. Such conditions occur when the depth to the seamount is of the order of 1 hydroacoustic wavelength or less and as a result, the ocean-atmosphere interface becomes anomalously transparent (Godin, 2008). Infrasound, used as a verification technique for the Comprehensive Nuclear-Test-Ban Treaty (CTBT), is also a sensitive probe of the upper atmosphere (Smets et al., 2016).

Understanding seismic-to-infrasonic coupling is important for characterizing sources in the subsurface. Assink et al. (2016) have used infrasound detections of the 2013 and 2016 underground nuclear tests by the Democratic People's Republic of Korea in order to further constrain source depth, which is difficult to estimate from seismic data alone. Whitaker and Mutschlecner (2008) and Mutschlecner and Whitaker (2005) have

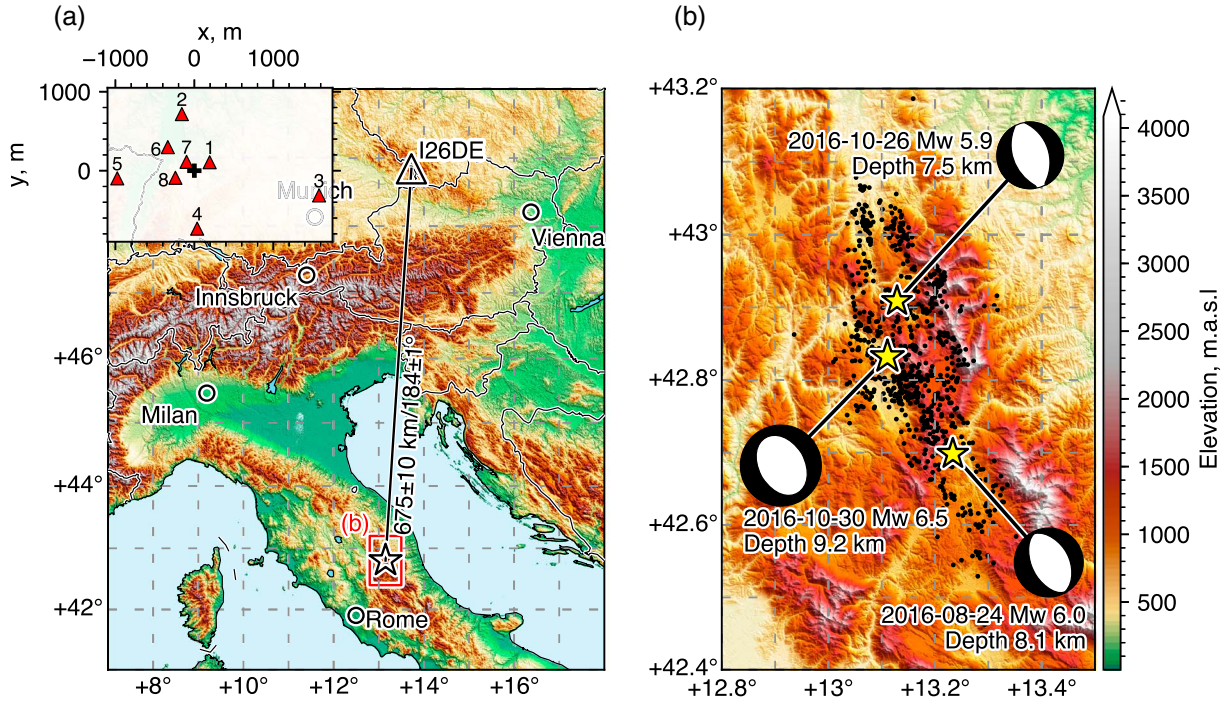

Figure 1. Earthquake sequence in central Italy, August–December 2016. (a) Overview map with shaded relief of surface topography from Advanced Spaceborne Thermal Emission and Reflection Radiometer Global Digital Elevation Model version 2 (ASTER-GDEM2 is a product of NASA and METI, Tachikawa et al., 2011). Epicentral region is marked by a star; station I26DE is marked by a triangle. I26DE microbarometer configuration presented in inset frame. (b) Zoom-in on the epicentral region: Mainshocks discussed in the current paper are marked by yellow stars; aftershocks are marked by black dots. Moment tensor solutions from Istituto Nazionale di Geofisica e Vulcanologia (INGV) (2016) (http://cnt.rm.ingv.it/tdmt, last accessed November 2017).

investigated infrasound signals from explosions and earthquakes and formulated signal amplitude and duration versus yield or magnitude relations.

In the period between August and December 2016, central Italy has been hit by several mainshocks followed by hundreds of aftershocks along a 60 km long Apenninic-trending normal-fault system (Cheloni et al., 2017; Chiaraluce et al., 2017)(see Figure 1). Discussed in this paper are three mainshocks marked by stars in Figure 1b. In chronological order, the earthquakes are as follows: (a) the M_w 6.0 Amatrice earthquake with UTC origin time 24 August 2016 01:36:32, (b) the M_w 5.9 Visso earthquake with UTC origin time 26 October 2016 19:18:05, and (c) the M_w 6.5 Norcia earthquake with UTC origin time 30 October 2016 06:40:17. Earthquake source parameters are thoroughly discussed by Chiaraluce et al. (2017) and (Cheloni et al., 2017); however, it is noted that all three earthquakes have relatively similar moment tensor solutions. With hypocentral depth between 7 and 9.5 km (Figure 1b) these mainshocks are relatively shallow. Shallow seismic sources tend to generate large-amplitude ground motions and are likely to generate large-amplitude infrasound as well.

Besides seismic signal detections on local and global seismic networks, this sequence generated infrasonic signals detectable at station I26DE (Freyung, Germany, Figure 1a) of the International Monitoring System (IMS) (Dahlman et al., 2009). Constructed as part of the verification measures for the CTBT, I26DE is at a source-receiver distance from the mainshocks of 675 ± 10 km. Unlike the elastic medium, which remains constant in time, atmospheric conditions change rapidly. The detectability of infrasound at large propagation distances (>200 km) highly depends on the state of the stratosphere (Assink, Waxler, et al., 2014; Waxler et al., 2015).

The propagation velocity of (infra-)sound in the atmosphere depends on temperature and wind but typically revolves around a *celerity* (average propagation velocity; propagation range divided by travel time) of 0.3 km/s on average over long ground-to-ground propagation paths (Evers & Haak, 2007). Atmospheric wind along the propagation path may expedite travel times if in the direction of propagation, leading to celerities as high as 0.36 km/s. Wind may also prolong travel time and even prohibit ground-to-ground stratospheric propagation altogether if in the opposite direction.

In what follows, we first describe the data processing and observations at I26DE. We go on to demonstrate two independent backprojection methodologies and results, outlining the regions in which seismic waves couple to the atmosphere and produce infrasound. We conclude with a discussion of our findings and convey a new understanding of the seismoacoustical coupling process.

2. Data Processing and Observations

I26DE is an eight-element array. It is equipped with MB2005 microbarometric sensors, which are sensitive to pressure fluctuations as well as mechanical vibrations, connected to a pipe array at the surface for wind-noise reduction (Ponceau & Bosca, 2010). It has a maximum aperture of 2,565 m, and pressure data are continuously recorded at each element at a sampling rate of 20 Hz. Such array configuration allows for the accurate estimation of the back azimuth and apparent velocity of an incident acoustic wave in the frequency range of 0.1 to 5 Hz. Recordings are trimmed to 3 min before and 70 min after event origin time, which allows ample time for infrasound to reach the station. We detrended and de-mean the signal to remain with pressure fluctuations around a mean value. A taper is applied to the beginning and end of the signal, which is then band-pass filtered (0.3–3 Hz for Amatrice earthquake and 0.5–3 Hz for Visso and Norcia earthquakes). This avoids contamination of low frequencies by microbaroms, around 0.2 Hz, and high frequencies by resonance in the pipe array (Hedlin & Raspet, 2003).

For array processing, we employ a Fisher detector, which gives a measure of the signal coherency as a result of different time shifts in overlapping time bins (Melton & Bailey, 1957). A sliding window of 20 s with an overlap of 95% was chosen to allow the slowest propagating infrasonic wavefront to propagate through the elements of the array. Coherent signals propagating over the array have a higher Fisher (F-)ratio than incoherent, uncorrelated noise. The F-ratio is a sensitive measure of the signal coherency or signal-to-noise ratio (SNR) (Melton & Bailey, 1957), where $\mathrm{SNR} = \sqrt{(\text{F-ratio} - 1)/N}$ and N is the number of instruments included in the beamforming.

In our beamforming analysis, we have constructed a slowness grid spanning a back azimuth range from 0° to 360° in steps of 2° and an apparent velocity range from 0.28 to 6 km/s, covering both seismic and acoustic propagation speeds. For numerical efficiency, the apparent velocity grid is linearly spaced between 280 to 600 m/s in steps of 5 m/s and logarithmically spaced above 600 m/s. The best beam is constructed by summing and averaging all time-aligned traces with slowness parameters that give the maximal F-ratio in the overlapping bins. This process reduces the incoherent noise due to wind and turbulence and increases the signal due to coherent wavefronts.

The back azimuth and the apparent velocity are also determined from the slowness that maximizes the F-ratio. Back azimuth is the direction from which the coherent wavefront is arriving, and apparent velocity is its horizontal propagation velocity across the array. Apparent velocity is often used as a measure of the angle of incidence of the wavefront. In this study we use apparent velocity and celerity to discriminate between infrasound and seismic waves.

Figure 2 summarizes array processing results for recording of (a) the M_w 6.0 Amatrice earthquake, (b) the M_w 5.9 Visso earthquake, and (c) the M_w 6.5 Norcia earthquake. Origin time and location of events is retrieved from the Istituto Nazionale di Geofisica e Vulcanologia (INGV) catalog (INGV, 2016). The time axis on the bottom is relative to origin time, and the celerity scale at the top of best beam plot is the distance of I26DE from the event origin divided by time of arrival relative to origin time, which corresponds to travel time. Two distinct signals originating at the earthquake source or epicentral region are detected; (1) A seismic signal consisting of body and surface phases is detected with a celerity range of ~6 to ~2 km/s, and (2) an infrasound signal is detected with a celerity range of ~0.35 to ~0.22 km/s. However, a third type of signal is seen as well. This signal arrives after the seismic detections and before the epicentral infrasound detections with a celerity of ~1 km/s. This intermediate signal, as well as the epicentral infrasound signal, traverses the array with an apparent velocity of roughly 0.35 km/s. Relative to the epicentral infrasound detections, which exhibit a stable back azimuth pointing toward the epicenter, the intermediate signal detections are scattered with ±35°. The three signals are marked in Figure 2.

The apparent velocity of the intermediate signal indicates that it is infrasound but the celerity, which is 3 times the speed of sound, is too fast for it to originate at the epicenter. Therefore, this intermediate infrasound signal must have a propagation path, which is part seismic and part atmospheric. The region where seismic ground

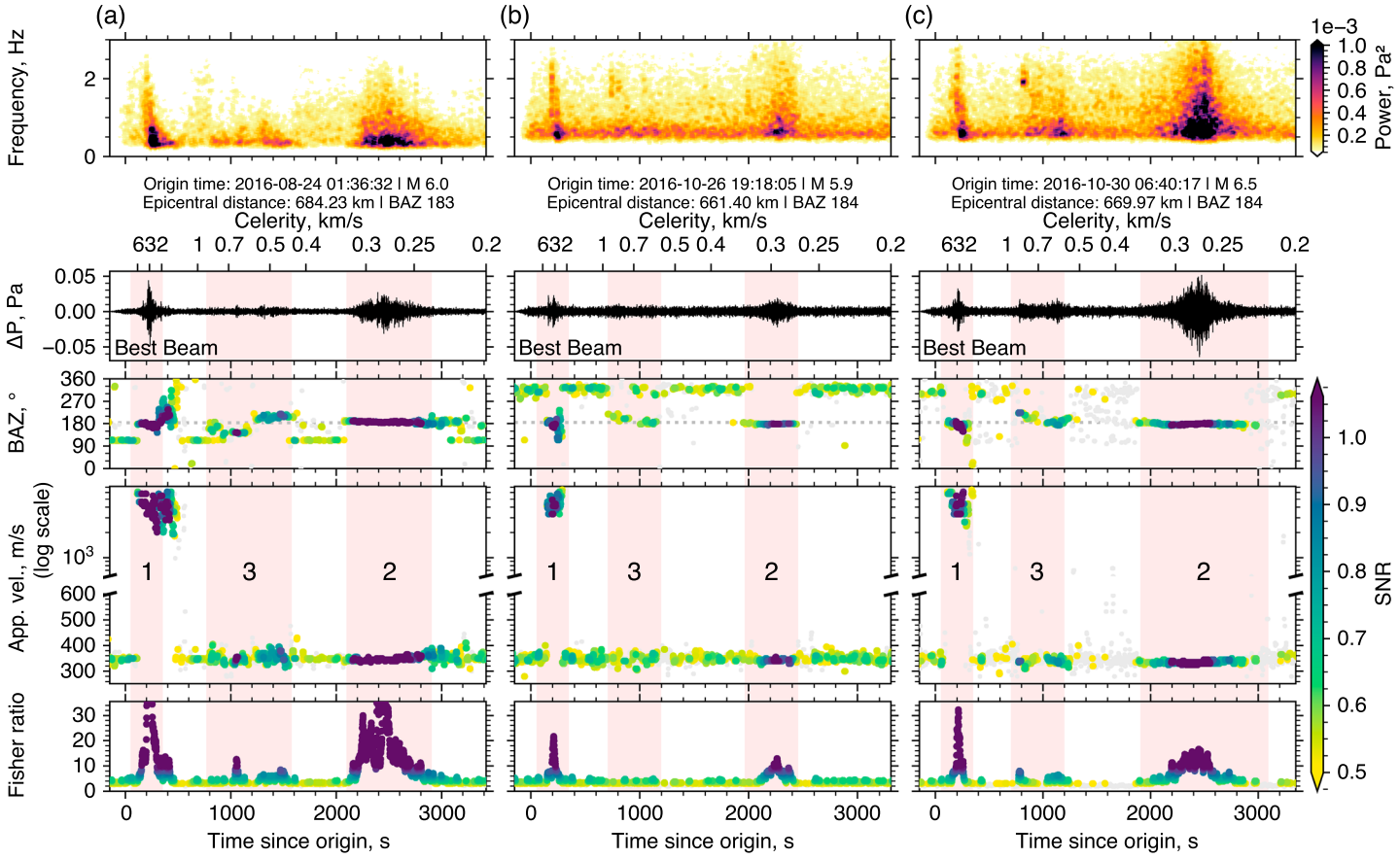

Figure 2. Beamforming results using infrasonic recordings of I26DE for (a) Amatrice earthquake, (b) Visso earthquake, and (c) Norcia earthquake. From top to bottom, frames are the following: spectrogram of the best beam, the best beam time history of the pressure fluctuations, back azimuth in degrees (true back azimuth as dotted gray line), apparent velocity (linear below 600 m/s, logarithmic above that), and Fisher ratio of the detections. Results are color coded by SNR. Marked in each frame are (1) seismic signal, (2) epicentral infrasound, and (3) intermediate infrasound.

motions couple to the atmosphere and generates infrasound waves is a secondary infrasound source and is the focus of this research.

3. Atmosphere-Independent Backprojection

In order to approximate the location of the secondary and epicentral infrasound sources, we simultaneously minimize the misfit in travel time and back azimuth. We follow a simplified approach, similar to that described by Marchetti et al. (2016) and Arrowsmith et al. (2009). Assuming that the highest-amplitude phases of the seismic waves contribute the highest pressure perturbations in the atmosphere, we approximate constant seismic surface wave propagation velocity of 3 km/s. This is in agreement with the celerity of the peak of the seismic phases detected at I26DE as shown in Figure 2. We also approximate constant infrasound propagation velocity of 0.3 km/s, also in agreement with epicentral infrasound detections at I26DE (see Figure 2). A travel time matrix, T_{ij}, and a back azimuth matrix, BAZ_{ij}, are constructed at 0.05° grid spacing over the extent of the map in Figure 1. Every grid point (i, j) is treated as a potential point at which seismic waves may couple to infrasound. T_{ij} is therefore the sum of the seismic travel time, Ts_{ij}, from the hypocenter to each grid point:

$$Ts_{ij} = \left(h^2 + Rs_{ij}^2\right)^{0.5} / c_s, \tag{1}$$

and Ti_{ij}, the infrasonic travel time from that grid point to I26DE:

$$Ti_{ij} = Ri_{ij} / c_i, \tag{2}$$

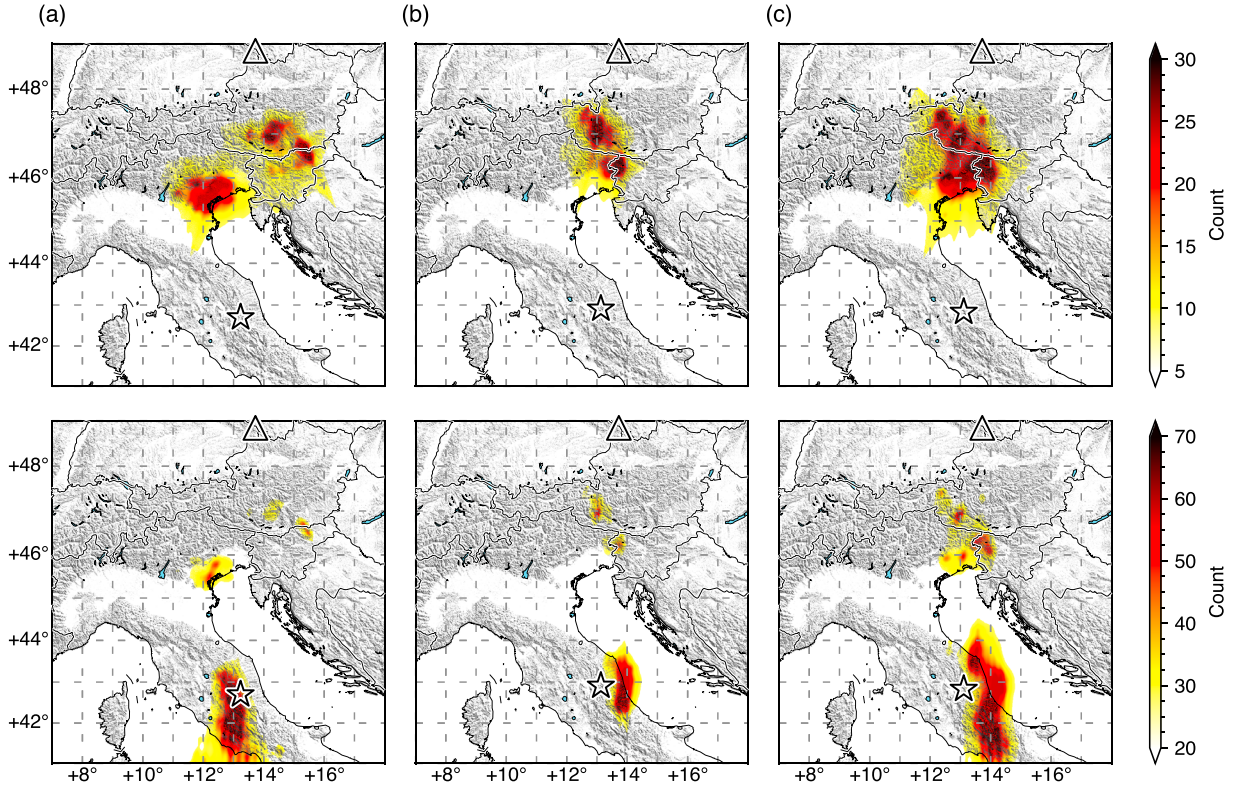

Figure 3. Backprojection of time and back azimuth detections for (a) Amatrice earthquake, (b) Visso earthquake, and (c) Norcia earhtquake. Top row presents backprojections using (only) the intermediate infrasound detections. Bottom row presents backprojections using all detections. Color coding by count of detections that originate in each cell of the searched grid. Epicenter is marked by a star; I26DE is marked by a triangle.

where h is the hypocentral depth of the event, Rs_{ij} and Ri_{ij} are horizontal distance along a great circle of the seismic and infrasonic paths, respectively, and c_s and c_i are seismic and infrasonic propagation velocities. Back azimuth to each point is

$$\mathrm{BAZ}_{ij} = \arctan\left(\frac{(\sin(\phi_a - \phi_{ij})\cos(\phi_a))}{\cos(\lambda_{ij})\sin(\lambda_a) - \sin(\lambda_{ij})\cos(\lambda_a)\cos(\phi_a - \phi_{ij})}\right), \tag{3}$$

λ_{ij}, ϕ_{ij} are the latitude and longitude of a given point (i, j), and λ_a, ϕ_a are the central coordinates of the array.

For each back azimuth detection point, BAZ_d at time T_d, we evaluate the joint normalized misfit M to be

$$M = \frac{M\mathrm{baz}_{ij}}{\max(M\mathrm{baz}_{ij})} \cdot \frac{Mt_{ij}}{\max(Mt_{ij})}, \tag{4}$$

where $M\mathrm{baz}_{ij} = |\mathrm{BAZ}_{ij} - \mathrm{BAZ}_d|$ and $Mt_{ij} = |T_{ij} - T_d|$ are the back azimuth and travel time residual matrices, respectively. The grid point (i, j) which corresponds to $\min(M)$ is then most likely the point at which an infrasound detection with back azimuth, BAZ_d at time T_d, originated from. A count of the number of detections originating from each grid point is kept and plotted for each of the three events in Figure 3. The top row in Figure 3 presents backprojections using (only) the intermediate infrasound detections, and the bottom row presents backprojections using all infrasound detections.

This approach does not account for any atmospheric effects such as velocity of the wind components and temperature variations that affect sound speeds and may result in inaccurate locations. The longer the propagation range, the more this approach is prone to error. The manifestation of such errors is visible in the bottom frame of Figures 3b and 3c as the epicentral infrasound patch is offset to the east relative to the true epicenter. This is due to stratospheric crosswinds along the propagation path, which leads to a discrepancy in back azimuth. The eastern offset from the epicenter of the October earthquakes is explained by the eastward stratospheric vortex, which has turned to its winter state after the equinox (Smets et al., 2015). At short propagation ranges, however, the expected error is of lesser extent. Note that for the Amatrice earthquake,

which occurs in late August as equinox approaches, stratospheric zonal winds are weaker and this approach works well for the epicentral infrasound patch as well.

For the Amatrice earthquake (Figure 3a) the secondary infrasound patch is split into two subpatches: (1) in the Northern part of the Padan Plain in Northern Italy and (2) in the more mountainous region of the Austrian Alps. Marchetti et al. (2016) have shown that for an earthquake underneath the Po Plain (included in the Padan Plain), the interaction of seismic waves with alluvial sediments generates large infrasound radiation. It is also plausible that for earthquakes outside the Po Plain, seismic wave interaction with such sediments may generate large infrasound radiation due to ground motion amplification and prolonged shaking in soft, unconsolidated sediments.

For the Visso and Noricia earthquakes (Figures 3b and 3c), the secondary infrasound patch is mainly in the mountainous region of the Austrian and Julian Alps. Darker spots with higher detection counts are seen above the Ankogel Group, Venediger Group, Glockner Group, and other parts of the High Tauern mountain range and above the Triglav mountain in Slovenia. Le Pichon et al. (2003, 2005, 2006), Mutschlecner and Whitaker (2005), Green et al. (2009), and others have shown examples of secondary infrasound generated by interaction of seismic waves with steep topographic reliefs.

Note that for the Noricia earthquake, in addition to infrasound radiating from mountain ranges, the secondary infrasound patch seems to extend to the same region of the Padan Plain depicted by the secondary infrasound patch of the Amatrice earthquake.

How is it that earthquakes of similar source characteristics, that is, focal mechanism, magnitude, location, and depth, recorded at the same array, have apparently different seismoacoustic coupling mechanisms and secondary source patches in different locations? To answer this question, we look at the state of the atmosphere.

4. Three-Dimensional Ray Tracing Through the Atmosphere

We recall that the backprojection approach described above is "unaware" of the state of the atmosphere. In what follows, we backproject rays using three-dimensional (3-D) ray tracing through atmospheric conditions reaching an altitude of ~80 km (1 Pa) obtained from the European Centre for Medium-Range Weather Forecasts (ECMWF). An in-house developed ray tracing algorithm, cast in spherical coordinates, that accounts for the full effect of the 3-D inhomogeneous wind and temperature fields is used (e.g., Smets et al., 2015, 2016). Realistic topography is also accounted for using 1 arc min global relief model (ETOPO1, Amante & Eakins, 2009). Rays are launched at the central coordinates of the array toward the epicenter over an azimuth range of $\pm 40^\circ$ of the true back azimuth at 1° azimuthal spacing and at elevation angels of 0° to 25° every 2° above the horizontal. In order to facilitate backward propagation of the rays from the array, horizontal components of the wind are reversed.

Figure 4 summarizes the results for the Visso (Figure 4a) and Norcia earthquakes (Figure 4b). Top view of raypaths are presented in the maps in Figure 4. As ray theory is a high-frequency approximation of the wavefield, we set a threshold of two acoustic wavelengths above the topographic surface and consider this to be close enough to act as a bounce point. The effectiveness of waveguide, or *duct*, with regard to propagation of an infrasonic signal from source to receiver is described by the transmission loss. Transmission loss, approximated here by geometrical spreading only, is obtained from the Jacobian determinant of the ray equations.

We overlay the contours of the epicentral and secondary infrasound patches from Figure 3 on top of the bounce points and raypaths in Figure 4. The broad-scale features of the secondary infrasound patch as depicted by the detections-driven, atmosphere-independent backprojections, are reproduced by atmospheric conditions-driven backprojections using full 3-D ray tracing. The first bounce points overlap with the regions that have the highest detection counts with subsequent bounce points, farther away, making fewer contributions. Bounce points in Figure 4 are color coded by total travel time. That is, seismic travel time to each bounce point, calculated as before with a constant propagation velocity of 3 km/s, added to the infrasonic travel time computed by the ray tracing algorithm.

We note that for the Amatrice earthquake, neither 3-D ray tracing nor full-wave propagation modeling (not shown here) can adequately explain the observed infrasound. Figure S1 in the supporting information presents similar information for the Amatrice earthquake as presented for the Visso and Norcia earthquakes in Figure 4. The reader is referred to the supporting information accompanying this paper for further discussion.

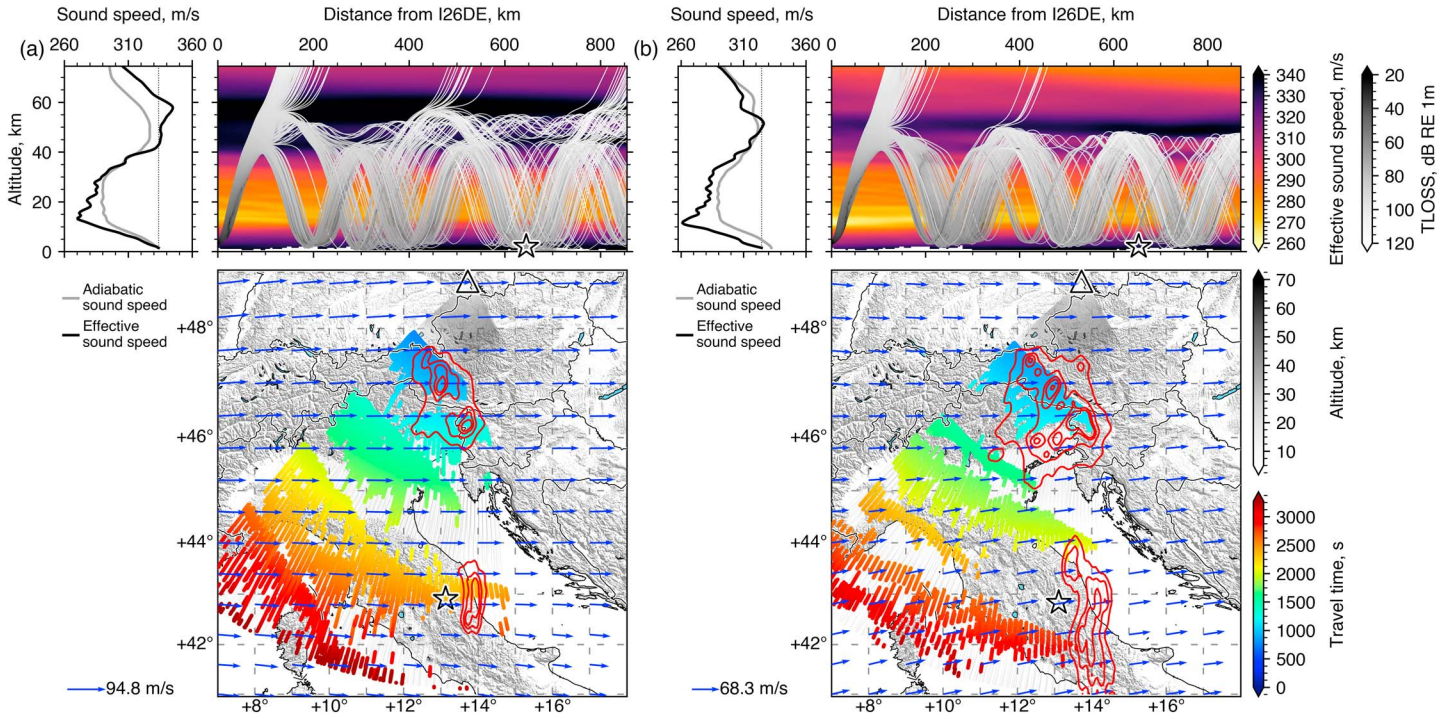

Figure 4. Backprojections using 3-D ray tracing through high-resolution atmospheric conditions available from ECMWF. (a) Visso earthquake and (b) Norcia earthquake. Top left: adiabatic (gray) and effective (black) sound speed at I26DE. Top: vertical cross section of effective sound speed showing rays along back azimuth ±10° color coded by transmission loss. bottom: map showing ray tracks color coded by altitude and near- or at-ground reflection points color coded by travel time. Blue arrows show horizontal wind strength and direction at 50 km altitude. Contours of the epicentral and secondary infrasound source areas from Figure 3 are overlaid in red.

In order to quantify the agreement between the two secondary infrasound patches outlined by the different backprojection procedures, we compare the back azimuth and time of detections to the back azimuth and travel time associated with each bounce point generated by the ray tracing approach. For each back azimuth detection, BAZ_d at time T_d, we find the bounce point P_b with back azimuth BAZ_b (see equation (3)) and travel time T_b that has the lowest back azimuth residual, $BAZ_r = \min(|BAZ_d - BAZ_b|)$, and lowest travel time residual, $T_r = \min(|T_d - T_b|)$. Bounce points with back azimuth residuals larger than ±2° and travel time residuals larger than ±2 s are rejected. The goodness of fit (GOF) is then evaluated by dividing the number of remaining bounce points by the root-mean-square of the residuals. Higher values represent better fit.

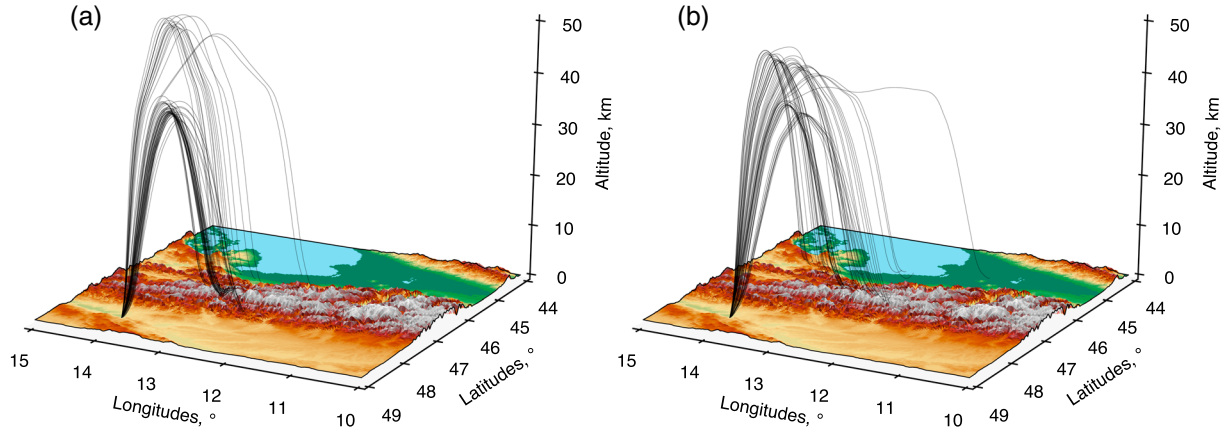

Figure 5. Eigenrays from secondary infrasound source to I26DE using 3-D ray tracing through high-resolution ECMWF atmospheric conditions. (a) Visso earthquake and (b) Norcia earthquake.

This process is repeated for all members of the ECMWF's ensemble of perturbed analyses (Smets et al., 2015). Shown in Figure 4 are ensemble member 8 of the 2016-10-26T18:00:00 analyses for the Visso event and ensemble member 0 of the 2016-10-30T06:00:00 analyses for the Norcia event. Both are the closest in time available products (±1.5 h of the corresponding event) and provide the highest GOF. Figure 5 presents eigenrays between the collection of bounce points that makes up the secondary infrasound source and I26DE.

5. Discussion and Conclusions

The manifestation of an intermediate, apparently fast-arriving infrasound signal occurs when ground motions over a secondary source region are efficiently coupled to an existing atmospheric duct connecting the secondary source region and the infrasound array. Propagation modeling indicates that the first bounce region from the array, yielding the lowest transmission loss, is favorable in that sense. Additional information about the state of the atmosphere can be inferred by approximating the secondary source region using backprojection of intermediate infrasound detections.

We note that the duration of the epicentral infrasound signals in Figure 2, correlates to the earthquake magnitude. For the M_w 6.0 Amatrice earthquake, epicentral infrasound signal lasts ~900 s. For the M_w 5.9 Visso earthquake, epicentral infrasound signal lasts ~600 s. For the M_w 6.5 Norcia earthquake, epicentral infrasound signal lasts ~1,200 s. These durations are consistent with the magnitude-duration relations proposed by Le Pichon et al. (2006) and Mutschlecner and Whitaker (2005). The duration of the intermediate infrasound signal is also proportional to the magnitude of the earthquake but is also affected by the efficiency of the atmospheric duct. This proportionality is in turn mapped to the spatial extent of the epicentral and secondary infrasound patches outlined by the detections-driven backprojection.

Epicentral infrasound observations (Figure 2) for all three earthquakes indicate that part of the infrasonic energy, which arrives with celerities <0.28 km/s, has propagated through the thermosphere. Infrasound radiation from southbound seismic wave propagation relative to the epicenter might also arrive later to an array north of the epicenter but this has a more limited effect.

During the Amatrice earthquake, although observations indicate that part of the infrasonic energy has propagated through the stratospheric waveguide, this could not be corroborated by either ray theory or full-wave propagation modeling. As similar observations have been made in earlier studies (Assink, Pichon, et al., 2014; Evers et al., 2012; Smets et al., 2015, 2016), understanding this discrepancy will be a topic of future study.

Understanding seismoacoustical coupling is of interest for the verification of the CTBT, where large underground explosions generate infrasound, which can be detected over long ranges (Assink et al., 2016). The fusion of seismic and infrasound data from underground sources will lead to better source characterization in terms of, for example, source depth and yield.

It is concluded that the different mechanisms described by Le Pichon et al. (2003, 2005, 2006), Marchetti et al. (2016), Mutschlecner and Whitaker (2005), and others for different earthquakes in different geological settings can coexist if the state of the atmosphere is considered; that is, they can all occur at the same time for the same earthquake if the state of the atmosphere can facilitate it. Generalizing this understanding, we infer that transmission of seismic waves in the elastic medium to infrasound in the acoustic medium may occur over a much larger region than previously described in the scientific literature but can only be observed where efficient atmospheric ducts to a receiver exists.

Acknowledgments
The data for this paper from CTBTO and ECMWF are available to member states but can be requested for academic purposes. The CTBTO and IMS station operators are thanked for the high-quality data and products. Infrasound data can be requested at the CTBTO International Data Center (IDC) in Vienna, via the virtual Data Exploration Center (vDEC, see https://www.ctbto.org/specials/vdec, last accessed: October 2017). Atmospheric data can be requested at the ECMWF via the Meteorological Archival and Retrieval System (MARS). Shahar Shani-Kadmiel's and Läslo Evers' contribution are funded through a VIDI project from the Netherlands Organization for Scientific Research (NWO), project 864.14.005. Pieter Smets is funded by the ARISE2 project from the European Commission H2020 program (grant 653980). Figures in this article are made with Matplotlib version 2.1.0 (Hunter, 2007).

References

Amante, C., & Eakins, B. W. (2009). ETOPO1 1 arc-minute global relief model: Procedures, data sources and analysis. NOAA Technical Memorandum NESDIS NGDC-24. National Geophysical Data Center, NOAA.

Arrowsmith, S. J., Burlacu, R., Whitaker, R., & Randall, G. (2009). A repeating secondary source of infrasound from the Wells, Nevada, earthquake sequence. *Geophysical Research Letters*, *36*, L11817. https://doi.org/10.1029/2009GL038363

Arrowsmith, S. J., Johnson, J. B., Drob, D. P., & Hedlin, M. A. H. (2010). The seismoacoustic wavefield: A new paradigm in studying geophysical phenomena. *Reviews of Geophysics*, *48*, RG4003. https://doi.org/10.1029/2010RG000335

Assink, J., Pichon, A., Blanc, E., Kallel, M., & Khemiri, L. (2014). Evaluation of wind and temperature profiles from ECMWF analysis on two hemispheres using volcanic infrasound. *Journal of Geophysical Research: Atmospheres*, *119*, 8659–8683. https://doi.org/10.1002/2014JD021632

Assink, J. D., Averbuch, G., Smets, P. S. M., & Evers, L. G. (2016). On the infrasound detected from the 2013 and 2016 DPRK's underground nuclear tests. *Geophysical Research Letters*, *43*, 3526–3533. https://doi.org/10.1002/2016GL068497

Assink, J. D., Waxler, R., Smets, P., & Evers, L. G. (2014). Bidirectional infrasonic ducts associated with sudden stratospheric warming events. *Journal of Geophysical Research: Atmospheres*, *119*, 1140–1153. https://doi.org/10.1002/2013JD021062

Cheloni, D., De Novellis, V., Albano, M., Antonioli, A., Anzidei, M., Atzori, S., … Doglioni, C. (2017). Geodetic model of the 2016 central Italy earthquake sequence inferred from InSAR and GPS data. *Geophysical Research Letters*, *44*, 6778–6787. https://doi.org/10.1002/2017GL073580

Chiaraluce, L., Di Stefano, R., Tinti, E., Scognamiglio, L., Michele, M., Casarotti, E., … Marzorati, S. (2017). The 2016 central Italy seismic sequence: A first look at the mainshocks, aftershocks, and source models. *Seismological Research Letters*, *88*, 757–771. https://doi.org/10.1785/0220160221

Cook, R. K. (1971). Infrasound radiated during the Montana earthquake of 1959 August 18. *Geophysical Journal International*, *26*, 191–198.

Dahlman, O., Mykkeltveit, S., & Haak, H. (2009). *Nuclear test ban: Converting political visions to reality*. Netherlands: Springer.

Donn, W. L., & Posmentier, E. S. (1964). Ground-coupled air waves from the Great Alaskan earthquake. *Journal of Geophysical Research*, *69*(24), 5357–5361.

Evers, L. G., Brown, D., Heaney, K. D., Assink, J. D., Smets, P. S. M., & Snellen, M. (2014). Evanescent wave coupling in a geophysical system: Airborne acoustic signals from the M_W 8.1 Macquarie Ridge earthquake. *Geophysical Research Letters*, *41*, 1644–1650. https://doi.org/10.1002/2013GL058801

Evers, L. G., Geyt, A. R. J., Smets, P. M. S., & Fricke, J. T. (2012). Anomalous infrasound propagation in a hot stratosphere and the existence of extremely small shadow zones. *Journal of Geophysical Research*, *117*, D06120. https://doi.org/10.1029/2011JD017014

Evers, L. G., & Haak, H. W. (2007). Infrasonic forerunners: Exceptionally fast acoustic phases. *Geophysical Research Letters*, *34*, L10806. https://doi.org/10.1029/2007GL029353

Godin, O. A. (2008). Sound transmission through water–air interfaces: New insights into an old problem. *Contemporary Physics*, *49*(2), 105–123.

Green, D. N., Guilbert, J., Le Pichon, A., Sebe, O., & Bowers, D. (2009). Modelling ground-to-air coupling for the shallow M_L 4.3 Folkestone, United Kingdom, earthquake of 28 April 2007. *Bulletin of the Seismological Society of America*, *99*(4), 2541–2551.

Hedlin, M. A. H., & Raspet, R. (2003). Infrasonic wind-noise reduction by barriers and spatial filters. *Journal of the Acoustical Society of America*, *114*(3), 1379–86.

Hunter, J. D. (2007). Matplotlib: A 2D graphics environment. *Computing In Science & Engineering*, *9*(3), 90–95.

Istituto Nazionale di Geofisica e Vulcanologia (INGV) (2016). ISIDe working group, version 1.0, doi:10.13127, ISIDe.

Le Pichon, A., Guilbert, J., Vallée, M., Dessa, J. X., & Ulziibat, M. (2003). Infrasonic imaging of the Kunlun Mountains for the great 2001 China earthquake. *Geophysical Research Letters*, *30*(15), 1095. https://doi.org/10.1029/2003GL017581

Le Pichon, A., Herry, P., Mialle, P., Vergoz, J., Brachet, N., Garcés, M., … Ceranna, L. (2005). Infrasound associated with 2004–2005 large Sumatra earthquakes and tsunami. *Geophysical Research Letters*, *32*, L19802. https://doi.org/10.1029/2005GL023893

Le Pichon, A., Mialle, P., Guilbert, J., & Vergoz, J. (2006). Multistation infrasonic observations of the Chilean earthquake of 2005 June 13. *Geophysical Journal International*, *167*(2), 838–844.

Marchetti, E., Lacanna, G., Le Pichon, A., Piccinini, D., & Ripepe, M. (2016). Evidence of large infrasonic radiation induced by earthquake interaction with alluvial sediments. *Seismological Research Letters*, *87*(3), 678–684.

Melton, B. S., & Bailey, L. F. (1957). Multiple signal correlators. *Geophysics*, *22*(3), 565–588.

Mutschlecner, J. P., & Whitaker, R. W. (2005). Infrasound from earthquakes. *Journal of Geophysical Research*, *110*, D01108. https://doi.org/10.1029/2004JD005067

Ponceau, D., & Bosca, L. (2010). Low-noise broadband microbarometers. In D. Ponceau, & L. Bosca (Eds.), *Infrasound monitoring for atmospheric studies* (pp. 119–140). Dordrecht: Springer.

Smets, P. S. M., Assink, J. D., Le Pichon, A., & Evers, L. G. (2016). ECMWF SSW forecast evaluation using infrasound. *Journal of Geophysical Research: Atmospheres*, *121*, 4637–4650. https://doi.org/10.1002/2015JD024251

Smets, P. S. M., Evers, L. G., Näsholm, S. P., & Gibbons, S. J. (2015). Probabilistic infrasound propagation using realistic atmospheric perturbations. *Geophysical Research Letters*, *42*, 6510–6517. https://doi.org/10.1002/2015GL064992

Tachikawa, T., Hato, M., Kaku, M., & Iwasaki, A. (2011). Characteristics of ASTER GDEM version 2. In *Geoscience and Remote Sensing Symposium (IGARSS), IEEE International. 24-29 July 2011* (pp. 3657–3660). Vancouver, BC.

Walker, K. T., Le Pichon, A., Kim, T. S., de Groot-Hedlin, C., Che, I. Y., & Garcés, M. (2013). An analysis of ground shaking and transmission loss from infrasound generated by the 2011 Tohoku earthquake. *Journal Of Geophysical Research: Atmospheres*, *118*, 831–851. https://doi.org/10.1002/2013JD020187

Waxler, R., Evers, L. G., Assink, J. D., & Blom, P. (2015). The stratospheric arrival pair in infrasound propagation. *Journal of the Acoustical Society of America*, *137*, 1846.

Whitaker, R. W., & Mutschlecner, J. P. (2008). A comparison of infrasound signals refracted from stratospheric and thermospheric altitudes. *Journal of Geophysical Research*, *113*, D08117. https://doi.org/10.1029/2007JD008852